Compact long-range single-photon underwater lidar with high spatial-temporal resolution

MINGJIA SHANGGUAN, [1,*] ZHIFENG YANG,[1] ZAIFA LIN[1], ZHONGPING LEE,[1] HAIYUN XIA[2], ZHENWU WENG[1]

[1] *State Key Laboratory of Marine Environmental Science, and Department of Applied Marine Physics & Engineering, College of Ocean and Earth Sciences, Xiamen University, Xiamen 361102, China*
[2] *School of Atmospheric Physics, Nanjing University of Information Science & Technology, 210044 Nanjing, China*
*mingjia@xmu.edu.cn

Received XX Month XXXX; revised XX Month, XXXX; accepted XX Month XXXX; posted XX Month XXXX (Doc. ID XXXXX); published XX Month XXXX

Oceanic lidar has emerged as a strong technology for oceanic three-dimensional remote sensing. However, most existing oceanic lidars are bulky and high power consumption, thus difficult to enable underwater operation. Here we present a compact single-photon lidar system for long-range underwater measurement. A single-photon detector was adopted to achieve a high signal-to-noise ratio. Benefiting from the single-photon sensitivity in detection, long-range active detection was realized with a low pulse energy laser at 1 μJ and a small-aperture coupler at 12 mm. Moreover, a narrow linewidth picosecond fiber laser with a high repetition rate was employed to guarantee a high spatial resolution and high update rate. A fiber-connected configuration in an optical receiver was specially designed for the miniaturized and robust structure. In an experimental demonstration, the profile of backscattered signal of water column up to 80 m with 1 s temporal and 5.6 cm spatial resolution was obtained to demonstrate the capability of this lidar system. The maximum detection distance of the single-photon lidar reaches $4.2/K_d$ (K_d, diffuse attenuation coefficient) for waterbody and up to $5.5/K_d$ for hard target. Furthermore, it exhibits a high update rate capability and realizes underwater bubbles detection up to 26 m away at a high update rate of 100 Hz. The results indicate its potential in a variety of applications such as remote sensing of marine biogeochemical parameters and long-range underwater imaging.

http://dx.doi.org/10.1364/OL.99.099999

Since lidar can operate at night, at high latitudes when solar radiation is low, and can potentially penetrate the subsurface chlorophyll maximum zone, it has become the most important technology to supplement passive ocean-color remote sensing, which has provided a sustained synoptic view of the distribution of ocean's optical properties and biogeochemical parameters for the past 20-plus years [1, 2]. By extracting depolarization, Brillouin, Raman and fluorescence information from the backscattering signal, oceanic lidar can retrieve a variety of parameters, including phytoplankton [3], temperature [4], bubbles [5], the dynamics of the upper ocean [6] and so on [7]. To improve detection capabilities, oceanic lidar have been deployed at different platforms, including underwater platforms [8] , surface vessels [9] , aircrafts [10] and satellites [11, 12]. However, most existing oceanic lidars are bulky and high on power consumption, where tremendous efforts have been devoted to the development of a compact oceanographic lidar for long-range active detection with high depth-temporal resolution, but it is still a challenging task.

On the one hand, researchers have developed several oceanic lidars with high pulse energy to penetrate more deeply [13]. With the pulse energy reaches the 100 mJ at 532 nm, oceanic lidar developed by the National Oceanic and Atmospheric Administration has revealed the thin scattering layers below 40 m in oceanic waters [6]. On the other hand, oceanic lidar based on blue light has been proposed since blue laser has a much better penetration depth in the open ocean than green laser. An airborne dual-wavelength oceanic lidar has demonstrated that the vertical profiles obtained by the 486 nm laser can penetrate approximately 100 m in the South China Sea, which is ~25% more than that of a 532 nm laser [14].

However, the scheme of increasing the pulse energy of the laser for deeper penetration has several significant drawbacks. Firstly, underwater plankton are subject to damage from high-energy laser, especially when the laser energy density is high in water, such as the application of shipborne or underwater lidar. Secondly, the eye safety is also a crucial factor that must be considered. Furthermore, high power consumption limits its operation on some important platforms, such as unmanned aerial vehicle or autonomous underwater vehicle (AUV). In addition, although blue laser can improve the detection performance of lidar, the requirements of high pulse energy and its more complex

structures limit its further application [15]. In view of that current oceanic lidars are high power consumption and bulky, a compact and low-power lidar system that can provide high spatial-temporal resolution profiles over long range with commercially available green laser is highly valuable, but not available yet. Fortunately, single-photon lidar has emerged as a strong candidate technology own to its high sensitivity. Although single photon detector technology has been widely used in atmospheric and target detection lidars [16-18], its application in oceanic lidars has rarely been reported, especially in underwater lidars. Since the penetration depth of laser in water is limited, a lidar operating underwater would greatly extend its performance, especially with the help of underwater platforms such as AUVs. In addition, interferences from the sea-air interface and atmospheric backscatter signal can be avoided, which is a great challenge for oceanic lidars that operate above the water [19].

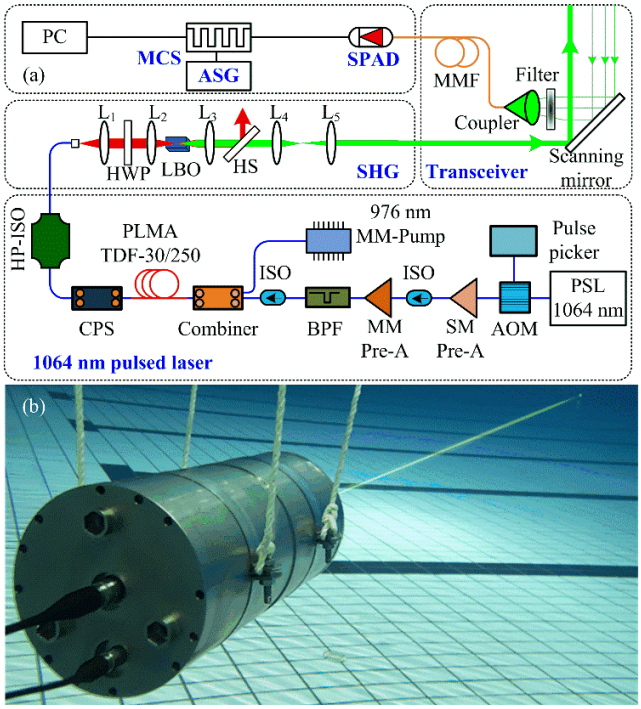

Fig. 1. (a) Schematic setup of the single-photon underwater lidar. MLFL, mode-locked fiber laser; FSM, frequency-selected model; WDM, wavelength division multiplexing; YDF: Ytterbium-Doped Fiber; ISO: isolator; PL: pump laser; HWP: half-wave plate; LBO: lithium borate; MMF: Multimode fiber; TDC: time digital converter; PC: personal computer. (b) Photograph of the underwater lidar

In this letter, we present a small-size single-photon oceanic lidar having underwater detection capabilities. To realize the long-range detection, we applied a single-photon detector to enhance the sensitivity of the lidar, so that low-power laser with a pulse energy of micropulse and a small-aperture coupler with aperture of cm can be applied. To realize high spatial resolution detection of underwater targets, we employed a picosecond pulse laser and a high precision time digital converter (TDC). This picosecond laser has the characteristics of high repetition rate, which enable the capability of high update rate detection. In this article, we demonstrate single-photon underwater detection at ranges up to 105 m with 5.5 cm spatial resolution and 1 s temporal resolution. Further, dynamic detection capability is demonstrated by monitoring underwater bubbles 26 m away from the lidar at the frequency of 100 Hz.

The schematic diagram of the single-photon lidar system setup is illustrated in Fig. 1. The system employs a compact fiber-based laser operating at 532 nm. The beam divergence of the laser is 0.5 mrad. A fiber-connected configuration is specially designed for the miniaturized and robust structure. The backscattered signal from the water is coupled in a 105-um MMF by a collimator with 27.5 mm focal length, which corresponds to the field of view (FOV) of 3.8 mrad. This narrow receiving FOV in our lidar system offered a significant backscattering noise suppression. The distance between the transmitted laser and received coupler is ~15 mm. A 532 nm filter with bandwidth of 0.2 nm is used to further block the background noise. Finally, a compact free-running silicon single-photon avalanche diode (SPAD) is adopted in our experiment. It has an efficiency of ~ 52 % with 100 dark counts per second (cps).

Table.1 Key parameters of the oceanic single-photon lidar

Parameter	Value
Pulsed Laser	
Wavelength (nm)	532
Pulse duration (ps)	501
Pulse energy (μJ)	1
Pulse repetition rate (MHz)	1
Beam divergence (mrad)	0.5
Coupler	
Aperture (mm)	12
Focal length (mm)	27.5
Mode-field diameter (μm)	105
FOV (mrad)	3.8
Silicon APD	
Detection efficiency at 532 (%)	52
Dark count (cps)	100

As to the electronic module, a homemade function generator (AFG) based on Field Programmable Gate Array (FPGA) provides precise control signal for laser, SPAD detector, TDC and scanning mirror. A high-precision TDC with 13 picosecond resolution is adopted to record the time of pulse emission and photon detection. Also, it records the start signal from motor controller that controls the scanning mirror to find the beginning of the data stream precisely. The time jitter of the whole system was measured at ~500 ps. A summary of the system parameters is listed in Table 1.

A photograph of the underwater lidar system is shown in Fig. 1(b). The lidar system is made of titanium alloy with high pressure resistance properties, so that the lidar can operate underwater up to 2 km. The optical window of the lidar is made of sapphire lens, which can maintain ≥ 96 % transmission under high pressure. The cylindrical lidar has a diameter of 20 cm and a length of 40 cm. The average power consumption of the lidar is less than 100 W. To enhance the spatial resolution and temporal resolution, a watt-

level, narrow-linewidth, all-polarization-maintaining (PM) green laser with repetition rate of 1 MHz is employed. Our picosecond green laser consists of a 1064 nm picosecond seed laser, a pulse picker, a master oscillator power amplifier (MOPA), and an LBO-based frequency doubling unit.

The picosecond seed laser is made by passively mode-locked all-PM Yb-fiber laser with 1063.92 nm central wavelength. The seed laser is then connected to a pulse picker, i.e., a synchronization-triggered acoustic-optical modulator (AOM), which acts as a frequency demultiplier to reduce the repetition rate to 1 MHz. The 1064 nm picosecond laser at 1 MHz repetition rate is further amplified by the MOPA. The MOPA is constructed by a single-mode (SM) Yb-doped fiber (YDF) pre-amplifier, a multi-mode (MM) YDF pre-amplifier and a main amplifier. The SM pre-amplifier uses a piece of single-clad PM YDF pumped by a 976 nm single-mode laser diode (LD). Then, the MM pre-amplifier comprises a 10 μm-core double-clad PM YDF pumped with a MM 976 nm LD using a fiber combiner. An average power of 250 mW can be generated after the second stage amplifier. To prevent the amplified spontaneous emission, a 0.5 nm bandpass filter (BPF) at 1064 nm is used in the output port of the MM pre-amplifier. At last, the main power amplifier is realized by a large-core double-clad PM YDF (30 μm core, NA=0.08; 250 μm inner-cladding, NA=0.46). A cladding power stripper (CPS) is adopted to remove the residual pump power, and a high-power optical isolator (HP-ISO) is used to protect the amplifier from possible damage caused by back-scattered light. Finally, up to 3.5 W of average power is achieved with a pulse duration of 501 ps and a repetition rate of 1 MHz.

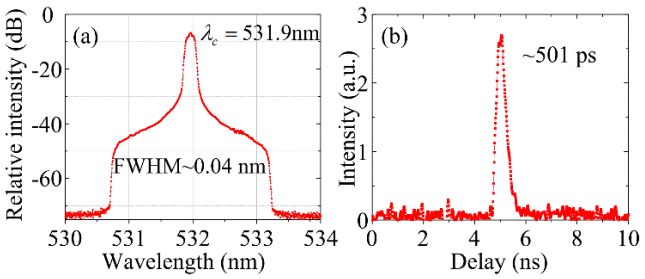

Fig. 3. Performance of the watt-level, narrow-linewidth all-PM picosecond green laser system. (a) Output optical spectrum. (b) Laser-pulse.

Subsequently, the frequency doubling from 1064 nm to 532 nm is carried out. The plane convex lens (L1) is employed to collimate the 1064 nm amplified laser from the FC/APC connector. The half-wave plate (HWP) adjusts the linearly polarization direction of the 1064 nm laser to meet the phase-matching condition of LBO crystal. The 1064 nm picosecond pulses are then focused onto the LBO crystal in a heat oven. Plane convex lens (L3) after LBO crystal is used to collimate the 532 nm green light, and a 45° harmonic separator (i.e., 532/1064 nm dichroic mirror) remove the residual 1064 nm laser. A pure green light at 531.96 nm is obtained. The average output power reaches 1 W. As shown in Fig. 3, the laser linewidth maintains a narrow one of 0.04 nm (full width of half maximum), and the pulse width is 501 ps. The pulse energy and peak power of the narrow-linewidth picosecond green laser enable 1 μJ and 2 kW, which could be very favorable to long-rang, high-resolution oceanic lidar.

Here we present a field experiment to demonstrate underwater performance including long-distance and high-speed underwater detection capabilities. A field experiment was carried out in a swimming pool at the Xiang'an campus of Xiamen University (2437′N, 11818′E). The size of the pool is 50×25×2 m^3.

To demonstrate that the detection distance of our lidar can be greater than 50 m, a 300×300 mm^2 mirror with high reflection at 532 nm was placed on the wall of the pool to reflect the laser. The raw profile with 1 s temporal resolution and 5.5 cm spatial resolution is plotted in Fig. 4. As shown there., the detection distance of waterbody backscattered signal is ~ 80 m, and the backscattered signal from the wall at a distance of ~ 105 m also detected. As the laser beam and the received FOV tends to overlap, the intensity of the backscattered signal first increases and then decreases with distance. Once the geometric overlap reaches 100 %, the backscattered signal decays exponentially from ~25 m. The first peak of the profile at ~ 51 m, which is due to the reflection of the high reflection mirror.

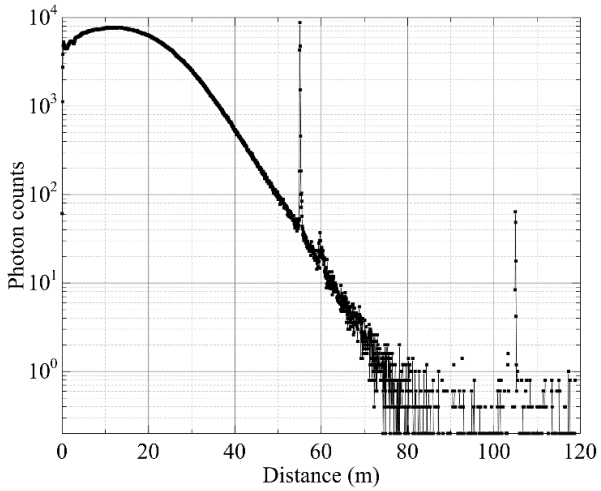

Fig. 4. Raw signals with 5.5 cm/1 s spatial/temporal resolution.

By using the ac-9 (Wet Labs) and HS6P (HOBI Labs), the absorption coefficient (a) and the backscattering coefficient (b_b) at 532 nm were measured simultaneously. The measured a, b_b, and c (beam attenuation coefficient) at 532 nm were 0.044 m^{-1}, 0.0035 m^{-1}, and 0.07 m^{-1}, respectively. The attenuation coefficient of the lidar (K_{lidar}), estimated with the traditional method from the profile slope, is about 0.064 m^{-1}, which is consistent with the conclusion that the K_{lidar} is approximately equal to c in the case of narrow receiver FOV [20]. With a diffuse attenuation coefficient model for K_d, where $K_d = m_0 \quad a + m_1[1 - m_2\exp(-m_3 a)b_b]$[21] and ($m_0$,$m_1$,$m_2$,$m_3$) are model parameters from Ref. 21, the estimated K_d is ~0.052 m^{-1}. Based on the measured results shown in Fig. 4, the detection range can reach ~4.2/K_d for this water body and up to 5.5/K_d for hard target. It is worth noting that most existing oceanic lidars have a penetration depth of only ~3/K_d, though high energy lasers at the 10 mJ level, or even 100 mJ level was used [6].

To demonstrate the robustness and flexibility of our lidar system, the lidar was switched to a scanning mode, where the beam is scanned by a scanning mirror, which is controlled by a

computer. As shown in Fig. 5, this single-photon lidar can precisely locate seven bubble sites generated by a bubble generator. The high update-rate detection capability of our lidar makes it possible to capture underwater moving objects. In the experiment, the fixed pointed lidar that transmitted a laser beam through a bubble at ~26 m away. The temporal resolution of the backscattered profile adjusts to 0.01 s (100 Hz update rate). As showing in Fig. 6, the number of bubbles passing through the laser beam per unit of time can be calculated, which is estimated as ~10 bubbles per second.

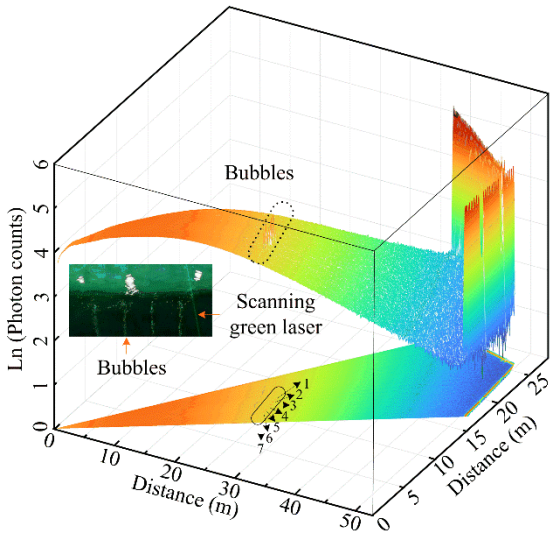

Fig. 5. Scanning pattern to locate bubbles in the swimming pool.

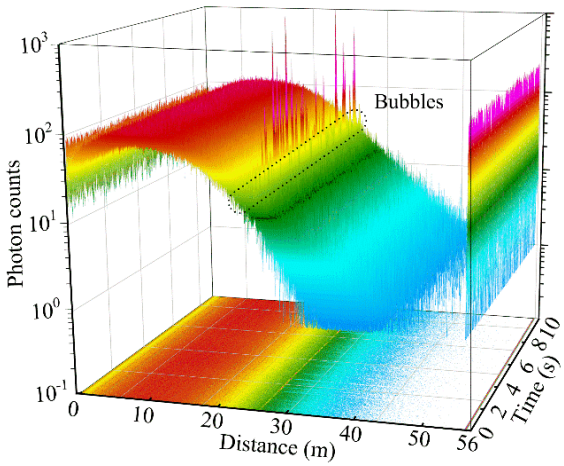

Fig. 6. Sensing the bubbles with the refresh rate of 100Hz.

In conclusion, based on a fiber-based picosecond laser and a single photon detector we developed a compact all-fiber single-photon underwater lidar with high spatial-temporal resolution. The field experiment demonstrated that this lidar has the long-range detection and high update-rate detection capabilities. The results suggest that single-photon lidar can be a powerful tool not only for mapping the spatial extent of thin scattering layers and linking their occurrence to larger scale physical processes, but also for tracking their evolution over time and guiding the ship-based sampling needed to understand their composition, dynamics, and impacts. In the following, we will focus on improving the performance of our lidar system such as the daytime operation, depolarization and fluorescence detection. Since the interference from the sea-air interface and atmospheric backscatter signals can be avoided, underwater lidar signals can potentially be used as true values to calibrate oceanic lidars above the water. Especially, this lidar will be deployed in AUVs, which will provide us with a new view to better understand the ocean biogeochemical cycle.

Funding. Natural Science Foundation of Fujian Province of China (No. 2020J01026); Joint Funds of the National Natural Science Foundation of China (No. U2106210); National Key Research and Development Program of China (2022YFB3901704); MEL-RLAB Joint Fund for Marine Science & Technology Innovation, and MEL Internal Research Program (MELRI2101).

Disclosures. The authors declare no conflicts of interest.

Data availability. The data that support the findings of this study are available from the corresponding author upon reasonable request.

References

1. C. A. Hostetler, M. J. Behrenfeld, Y. Hu, J. W. Hair, and J. A. Schulien, Annual review of marine science **10**, 121-147 (2018).
2. C. Jamet, A. Ibrahim, Z. Ahmad, F. Angelini, M. Babin, M. J. Behrenfeld, E. Boss, B. Cairns, J. Churnside, and J. Chowdhary, Frontiers in Marine Science **6**, 251 (2019).
3. S. Zhang and P. Chen, Optics Express **30**, 17665-17679 (2022).
4. A. Rudolf and T. Walther, Optical Engineering **53**, 051407 (2014).
5. J. H. Churnside, Optics express **18**, 8294-8299 (2010).
6. J. Churnside and L. Ostrovsky, International Journal of Remote Sensing **26**, 167-177 (2005).
7. J. H. Churnside and J. A. Shaw, Applied Optics **59**, C92-C99 (2020).
8. D. McLeod, J. Jacobson, M. Hardy, and C. Embry, in *2013 OCEANS-San Diego*, (IEEE, 2013), 1-8.
9. Y. Zhou, Y. Chen, H. Zhao, C. Jamet, D. Dionisi, M. Chami, P. Di Girolamo, J. H. Churnside, A. Malinka, and H. Zhao, Light: Science & Applications **11**, 1-13 (2022).
10. P. Chen, C. Jamet, Z. Zhang, Y. He, Z. Mao, D. Pan, T. Wang, D. Liu, and D. Yuan, Remote Sensing of Environment **263**, 112567 (2021).
11. X. Lu, Y. Hu, C. Trepte, S. Zeng, and J. H. Churnside, Journal of Geophysical Research: Oceans **119**, 4305-4317 (2014).
12. X. Lu, Y. Hu, Y. Yang, T. Neumann, A. Omar, R. Baize, M. Vaughan, S. Rodier, B. Getzewich, and P. Lucker, Earth and Space Science **8**, e2021EA001839 (2021).
13. B. L. Collister, R. C. Zimmerman, C. I. Sukenik, V. J. Hill, and W. M. Balch, Remote Sensing of Environment **215**, 85-96 (2018).
14. K. Li, Y. He, J. Ma, Z. Jiang, C. Hou, W. Chen, X. Zhu, P. Chen, J. Tang, and S. Wu, Remote Sensing **12**, 2844 (2020).
15. J. Ma, T. Lu, Y. He, Z. Jiang, C. Hou, K. Li, F. Liu, X. Zhu, and W. Chen, Applied Optics **59**, C87-C91 (2020).
16. M. Shangguan, H. Xia, C. Wang, J. Qiu, G. Shentu, Q. Zhang, X. Dou, and J.-w. Pan, Optics Express **24**, 19322-19336 (2016).
17. M. Shangguan, H. Xia, C. Wang, J. Qiu, S. Lin, X. Dou, Q. Zhang, and J.-W. Pan, Optics letters **42**, 3541-3544 (2017).
18. Z.-P. Li, X. Huang, Y. Cao, B. Wang, Y.-H. Li, W. Jin, C. Yu, J. Zhang, Q. Zhang, and C.-Z. Peng, Photonics Research **8**, 1532-1540 (2020).
19. X. Shen, W. Kong, P. Chen, T. Chen, G. Huang, and R. Shu, Remote Sensing **14**, 3351 (2022).
20. H. R. Gordon, Applied optics **21**, 2996-3001 (1982).
21. Z. P. Lee, K. P. Du, and R. Arnone, Journal of Geophysical Research: Oceans **110**(2005).

Uncategorized References

1. C. A. Hostetler, M. J. Behrenfeld, Y. Hu, J. W. Hair, and J. A. Schulien, "Spaceborne lidar in the study of marine systems," Annual review of marine science **10**, 121-147 (2018).
2. C. Jamet, A. Ibrahim, Z. Ahmad, F. Angelini, M. Babin, M. J. Behrenfeld, E. Boss, B. Cairns, J. Churnside, and J. Chowdhary, "Going beyond standard ocean color observations: lidar and polarimetry," Frontiers in Marine Science **6**, 251 (2019).
3. S. Zhang and P. Chen, "Subsurface phytoplankton vertical structure from lidar observation during SCS summer monsoon onset," Optics Express **30**, 17665-17679 (2022).
4. A. Rudolf and T. Walther, "Laboratory demonstration of a Brillouin lidar to remotely measure temperature profiles of the ocean," Optical Engineering **53**, 051407 (2014).
5. J. H. Churnside, "Lidar signature from bubbles in the sea," Optics express **18**, 8294-8299 (2010).
6. J. Churnside and L. Ostrovsky, "Lidar observation of a strongly nonlinear internal wave train in the Gulf of Alaska," International Journal of Remote Sensing **26**, 167-177 (2005).
7. J. H. Churnside and J. A. Shaw, "Lidar remote sensing of the aquatic environment," Applied Optics **59**, C92-C99 (2020).
8. D. McLeod, J. Jacobson, M. Hardy, and C. Embry, "Autonomous inspection using an underwater 3D LiDAR," in *2013 OCEANS-San Diego*, (IEEE, 2013), 1-8.
9. Y. Zhou, Y. Chen, H. Zhao, C. Jamet, D. Dionisi, M. Chami, P. Di Girolamo, J. H. Churnside, A. Malinka, and H. Zhao, "Shipborne oceanic high-spectral-resolution lidar for accurate estimation of seawater depth-resolved optical properties," Light: Science & Applications **11**, 1-13 (2022).
10. P. Chen, C. Jamet, Z. Zhang, Y. He, Z. Mao, D. Pan, T. Wang, D. Liu, and D. Yuan, "Vertical distribution of subsurface phytoplankton layer in South China Sea using airborne lidar," Remote Sensing of Environment **263**, 112567 (2021).
11. X. Lu, Y. Hu, C. Trepte, S. Zeng, and J. H. Churnside, "Ocean subsurface studies with the CALIPSO spaceborne lidar," Journal of Geophysical Research: Oceans **119**, 4305-4317 (2014).
12. X. Lu, Y. Hu, Y. Yang, T. Neumann, A. Omar, R. Baize, M. Vaughan, S. Rodier, B. Getzewich, and P. Lucker, "New Ocean Subsurface Optical Properties From Space Lidars: CALIOP/CALIPSO and ATLAS/ICESat‐2," Earth and Space Science **8**, e2021EA001839 (2021).
13. B. L. Collister, R. C. Zimmerman, C. I. Sukenik, V. J. Hill, and W. M. Balch, "Remote sensing of optical characteristics and particle distributions of the upper ocean using shipboard lidar," Remote Sensing of Environment **215**, 85-96 (2018).
14. K. Li, Y. He, J. Ma, Z. Jiang, C. Hou, W. Chen, X. Zhu, P. Chen, J. Tang, and S. Wu, "A dual-wavelength ocean lidar for vertical profiling of oceanic backscatter and attenuation," Remote Sensing **12**, 2844 (2020).
15. J. Ma, T. Lu, Y. He, Z. Jiang, C. Hou, K. Li, F. Liu, X. Zhu, and W. Chen, "Compact dual-wavelength blue-green laser for airborne ocean detection lidar," Applied Optics **59**, C87-C91 (2020).
16. M. Shangguan, H. Xia, C. Wang, J. Qiu, G. Shentu, Q. Zhang, X. Dou, and J.-w. Pan, "All-fiber upconversion high spectral resolution wind lidar using a Fabry-Perot interferometer," Optics Express **24**, 19322-19336 (2016).
17. M. Shangguan, H. Xia, C. Wang, J. Qiu, S. Lin, X. Dou, Q. Zhang, and J.-W. Pan, "Dual-frequency Doppler lidar for wind detection with a superconducting nanowire single-photon detector," Optics letters **42**, 3541-3544 (2017).
18. Z.-P. Li, X. Huang, Y. Cao, B. Wang, Y.-H. Li, W. Jin, C. Yu, J. Zhang, Q. Zhang, and C.-Z. Peng, "Single-photon computational 3D imaging at 45 km," Photonics Research **8**, 1532-1540 (2020).
19. X. Shen, W. Kong, P. Chen, T. Chen, G. Huang, and R. Shu, "A Shipborne Photon-Counting Lidar for Depth-Resolved Ocean Observation," Remote Sensing **14**, 3351 (2022).
20. H. R. Gordon, "Interpretation of airborne oceanic lidar: effects of multiple scattering," Applied optics **21**, 2996-3001 (1982).
21. Z. P. Lee, K. P. Du, and R. Arnone, "A model for the diffuse attenuation coefficient of downwelling irradiance," Journal of Geophysical Research: Oceans **110**(2005).